Stem Cell Reports
Article

ISSCR

OPEN ACCESS

Retinal Organoids from Pluripotent Stem Cells Efficiently Recapitulate Retinogenesis

Manuela Völkner,[1] Marlen Zschätzsch,[1] Maria Rostovskaya,[2] Rupert W. Overall,[3] Volker Busskamp,[3] Konstantinos Anastassiadis,[2] and Mike O. Karl[1,3,*]

[1]German Center for Neurodegenerative Diseases (DZNE) Dresden, 01307 Dresden, Germany
[2]Stem Cell Engineering, Biotechnology Center (BIOTEC), TU Dresden, 01307 Dresden, Germany
[3]CRTD - Center for Regenerative Therapies Dresden, Technische Universität Dresden, 01307 Dresden, Germany
*Correspondence: mike.karl@dzne.de
http://dx.doi.org/10.1016/j.stemcr.2016.03.001

SUMMARY

The plasticity of pluripotent stem cells provides new possibilities for studying development, degeneration, and regeneration. Protocols for the differentiation of retinal organoids from embryonic stem cells have been developed, which either recapitulate complete eyecup morphogenesis or maximize photoreceptor genesis. Here, we have developed a protocol for the efficient generation of large, 3D-stratified retinal organoids that does not require evagination of optic-vesicle-like structures, which so far limited the organoid yield. Analysis of gene expression in individual organoids, cell birthdating, and interorganoid variation indicate efficient, reproducible, and temporally regulated retinogenesis. Comparative analysis of a transgenic reporter for PAX6, a master regulator of retinogenesis, shows expression in similar cell types in mouse in vivo, and in mouse and human retinal organoids. Early or late Notch signaling inhibition forces cell differentiation, generating organoids enriched with cone or rod photoreceptors, respectively, demonstrating the power of our improved organoid system for future research in stem cell biology and regenerative medicine.

INTRODUCTION

Pluripotent embryonic stem cells (PSCs) facilitate research on mammalian neuronal development, neurodegenerative disorders, and regenerative therapies. It has been shown in the retina that developmental processes such as optic-vesicle (OV) and optic-cup (OC) morphogenesis and signaling cascades can be reproduced using mouse and human embryonic stem cells (mESCs and hESCs) (Eiraku et al., 2011; Nakano et al., 2012; Hiler et al., 2015; La Torre et al., 2015). Retinal organoid (Boucherie et al., 2013; Decembrini et al., 2014; Gonzalez-Cordero et al., 2013) and 2D culture approaches (Lamba et al., 2006; Osakada et al., 2008) have been used for cell replacement therapy studies because efficient derivation of sufficient numbers of integration-competent cells remains a major limitation for regenerative medicine. The first reports on cell-based disease-modeling approaches (Phillips et al., 2014), retinal neuronal morphogenesis (Busskamp et al., 2014), and function in organoids (Zhong et al., 2014) are promising. Yet, in this evolving field, benefits and limitations have not been fully explored and many questions remain.

For example, the question of efficient generation of large, stratified, retinal tissues has not been addressed. Sasai and colleagues pioneered a protocol that allows the self-organization of eyecup-like structures (Eiraku et al., 2011; Nakano et al., 2012). This entails a series of complex tissue interactions, such as eyefield evagination and subsequent invagination, resulting in neural retina opposed by retinal pigment epithelium (RPE). However, this protocol relies on the evagination of the neuroepithelium and its live visualization, preferably using transgenic RAX (retina and anterior neural fold homeobox) reporter gene expression, for reliable manual isolation of the prospective retinal organoids. RAX is part of a group of transcription factors sufficient and necessary for the specification of the eyefield, which gives rise to the eye primordia and the retina. Although eyefield formation has been shown to be efficient in mouse PSC lines, the yield of retinal organoids depends on and is highly limited by a low frequency of neuroepithelial evagination (Eiraku et al., 2011; Hiler et al., 2015). Others have adapted protocols to maximize and simplify rod photoreceptor production by omitting the evagination dissection step. This results in larger organoids, with retinal and non-retinal structures intertwined within the starting organoid, and comes at the expense of inner-retina cell types (Decembrini et al., 2014; Gonzalez-Cordero et al., 2013). Therefore, we speculated that unbiased neuroepithelium trisection at the eyefield stage overcomes these limitations and enables production of more numerous retinal organoids.

Another question is the heterogeneity within and between organoids, which seems common to all the protocols developed so far but has not yet been studied in detail. Several processes, such as progenitor proliferation, cell differentiation, and ontogenetic cell death, could be potential sources of organoid variation. Transgenic animals with fluorescently labeled cells have been instrumental in visualizing major processes in the developing and adult retina. However, it is unknown whether reporter expression is

comparable between retinal organoids and in vivo. Thus, we investigated PAX6 transgenic reporter expression to gain an insight into retinal organoidogenesis. PAX6 is a highly conserved master regulator of neurogenesis (Shaham et al., 2012), playing several roles in eye and retinal development, e.g., eyefield specification, stemness control, and cell-fate specification. PAX6 reporter expression might also provide an insight into the formation of retinal structure because it remains expressed in postmitotic horizontal and amacrine cells, whose synaptic processes are part of the outer and inner plexiform layer, respectively.

Here, we have developed a protocol to facilitate efficient organoidogenesis of large, complex, 3D retinas derived from wild-type mESCs without requiring the formation and isolation of OV/OC-like structures. Gene-expression profile analyses of individual organoids and retinal cell birthdating experiments indicate efficient, reproducible, and temporally regulated retinogenesis. We have established retinal organoidogenesis from mESC and hESC lines carrying a human *PAX6* transgenic GFP reporter, hPAX6GFP BAC, and respective transgenic mice to assess GFP-expressing cells in a comparative approach. Our results suggest that our protocol is a valuable addition to the existing organoid technologies, and will facilitate future retina research and regenerative medicine.

RESULTS

Identifying the Limitations of Retinal Organoidogenesis

Taking advantage of the original retina organoid protocol (Eiraku and Sasai, 2011; Eiraku et al., 2011), we started the investigation using our transgenic hPAX6GFP mESC reporter lines and the respective wild-type mESC (E14TG2a). We generated the hPAX6GFP mESC lines by transposon-mediated BAC transgenesis. The reporter is composed of the human *PAX6* gene, with a GFP inserted in exon 4, and contains genomic sequences 108 kb upstream and 9.5 kb downstream of the gene body (Figure S1A). Two mESC clones were selected and tested positive for expression of pluripotency markers (Figure S1B; unless otherwise stated, clone 1 was used hereafter). Upon aggregation, mESCs formed continuous epithelial structures by day (D) 4–5 (Figure 1A), and by D10 we detected the first expression of hPAX6GFP (Figure 1B). However, although organoids had expanded in size and formed a neuroepithelial structure, the frequency of OV formation was as low as had been reported previously (Eiraku and Sasai, 2011; Hiler et al., 2015), which severely limited the number of retinal organoids generated. Furthermore, we did not observe any two-walled OC-like morphologies as previously described (Figure S1C and Table S1; Eiraku and Sasai, 2011). The protocol with ongoing culture of entire starting aggregates led to large heterogeneous organoids with intertwined retinal and non-retinal structures and rosette formation at D21 (Figures S1D and S1F; Table S1), comparable with previous reports (Decembrini et al., 2014; Gonzalez-Cordero et al., 2013). Specifically, the inner retinal cell types were not well developed: this substantially limited retinal organoid research and hPAX6GFP reporter analysis.

To overcome the observed limitations and to enable efficient retinal organoidogenesis, we devised an approach (Figures 1C and S1E) based on the following data on eyefield formation and neuroepithelium evagination efficiency. PAX6 and NESTIN expression at D5 indicated development of a polarized neuroepithelium with the apical surface inside (Figures S2A and S2B). Between D5 and D10, efficient eyefield induction and retinal determination occurred based on expression of the eyefield transcription factors RAX, PAX6, and LHX2 in predominant parts of the majority of organoids (D7, 81% ± 10% RAX^+ organoids, N = 7, n > 10; unless stated otherwise, data are given as mean ± SD of organoids [n] scored for marker expression by immunostaining per independent experiment [N]; Figures 2A–2C). At the same time, eyefield regions self-patterned into presumptive RPE ($MITF^+$ $OTX2^+$ $VSX2^-$ RAX^-) and neural retina (RAX^+ $VSX2^+$ $MITF^-$ $OTX2^-$) regions, reminiscent of an OC-like stage in vivo. RAX^+ regions co-expressed VSX2, indicating the onset of retinogenesis, while regions adjacent to the RAX^+ $VSX2^+$ areas expressed RPE markers (Figures 2B, S2D, and S2E). However, OC-like morphology due to tissue invagination was not observed; rather, the RPE regions that lie adjacent to the neural retina part either within the organoid main body (Figure 2B) or at the base of an evagination (Figure S2E). This suggested that self-patterning of the eyefield into presumptive neural retina and RPE occurred at the molecular, but not structural, level.

Next, we tested whether the cell-seeding density influences the evagination and eyefield differentiation efficiency: lower (1,500–3,000/well) compared with higher (6,000–9,000/well) cell-seeding numbers led to a higher percentage of organoids developing one or more evaginations by D7 (Figures 2D and 2E). The majority of organoids generated from lower seeding densities had eyefield areas (80% ± 4% RAX^+, N = 4, n = 24 organoids per seeding density and independent experiment [N]; Figures 2D and 2F), whereas organoids from higher seeding densities rarely had RAX^+ (10% ± 4% RAX^+, N = 4, n = 24), but regularly $LHX2^+$ areas. RAX^+ eyefield regions ranged from small parts to almost the entire organoid neuroepithelium (Figures 2A, 2D, and S2C). These quantitative data confirm and extend previous observations (Decembrini et al., 2014; Eiraku and Sasai, 2011), showing that eyefield differentiation efficiency is highly dependent on cell-seeding densities. Our

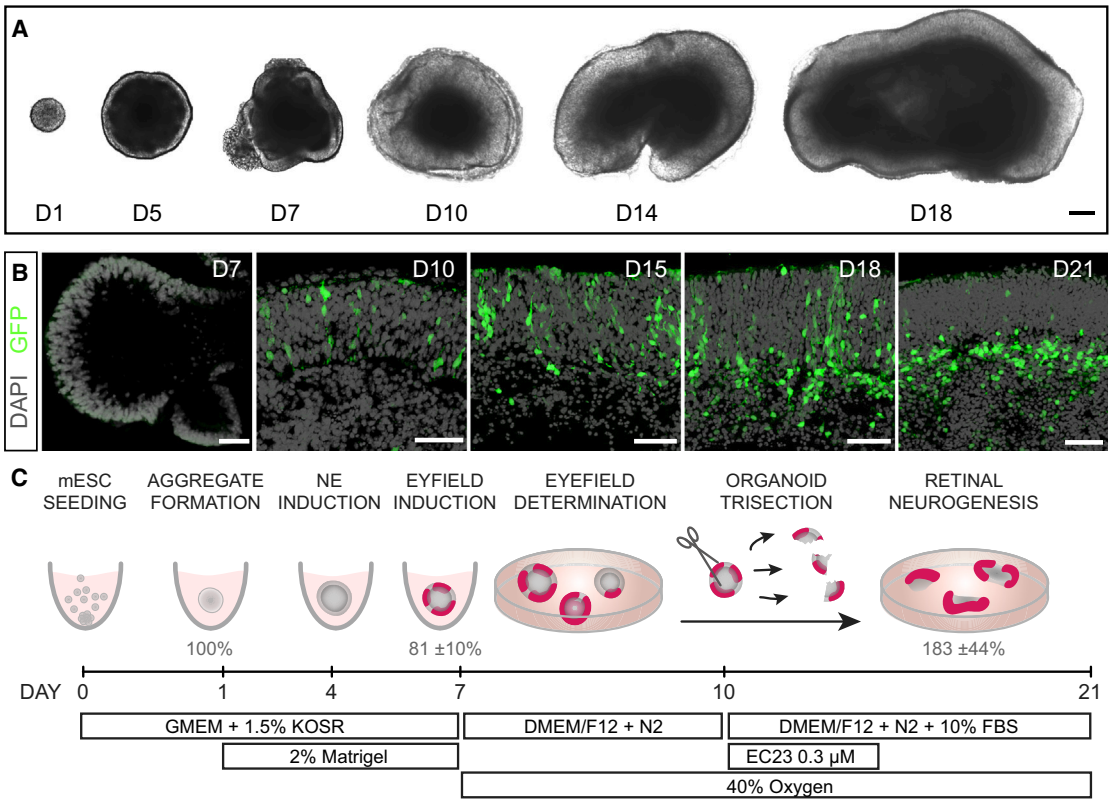

Figure 1. Description of the Retinal Organoidogenesis Trisection Protocol and the Generation of Wild-Type and hPAX6GFP mESC-Derived Retinal Organoids

(A and B) Representative phase contrast images of entire mESC-derived aggregates (A) and transgenic hPAX6GFP expression in organoid cryosections (B) at different days (D) of our trisection protocol. Aggregates are shown before (D1–10) and after (D14–18) organoid trisection.

(C) Schematic overview and timeline of the trisection protocol. mESC-derived starting (mother) aggregates are formed with 100% efficiency, out of which eyefield induction occurs in 81%, so that trisection increases the yield of retinal organoids to 183% ($N \geq 4$, $n \geq 20$). Magenta indicates eyefield tissue on D7–10 and retina thereafter. KOSR, knockout serum replacement; N2, N-2 supplement.

n = individual organoids per independent experiment (N). Scale bars, 200 μm (A) and 50 μm (B). See also Figure S1.

data indicate that aggregates with eyefield regions localized only in the aggregate main body were more frequent (65% ± 10%, n = 67) than aggregates with RAX^+ evaginations (35% ± 10%, N = 7, n = 67, $p < 0.0001$). Moreover, not all evaginations expressed eyefield markers (31% ± 7% RAX^-, 69% ± 7% RAX^+, N = 7, n = 57 evaginations analyzed; Figures 2G and S2C). Following the former protocol (Figures S1C and 2G) only 28% ± 8% (n = 25) of the starting aggregates could be used to harvest OV-like tissue, although their disposed main bodies frequently contained eyefield tissue. In addition, the majority of the starting organoids developed eyefield neuroepithelia within the main body without ever evaginating (53% ± 8%, N = 7, n = 42, $p < 0.0001$). These data imply that the default selection for evaginations omits numerous eyefield regions within mother aggregates. Consequently, merely isolating evaginations is a waste of potential retinal tissue. Also, evaginations are not reliable eyefield predictors. We reasoned that unbiased manual dissection of organoids at the eyefield stage into three evenly sized independent portions (trisection step), with potentially all of them containing eyefield-determined neuroepithelium, could enable the growth of three retinal organoids per starting aggregate (Figures S1E, 2G, and S2C).

Efficient Retinal Organoidogenesis from mESC

Following neuroepithelium trisection, the majority of organoids developed into large, continuous epithelial structures, resulting in the efficient formation of high numbers of large, stratified retinal organoids within 21 days (Figures 1, 2, 3, and S3; Table S1). Immunostaining analysis revealed organoid commitment to retinal fate, and indicated a synchronized onset and progression of retinogenesis. Quantitative analysis of cell proliferation and expression of the

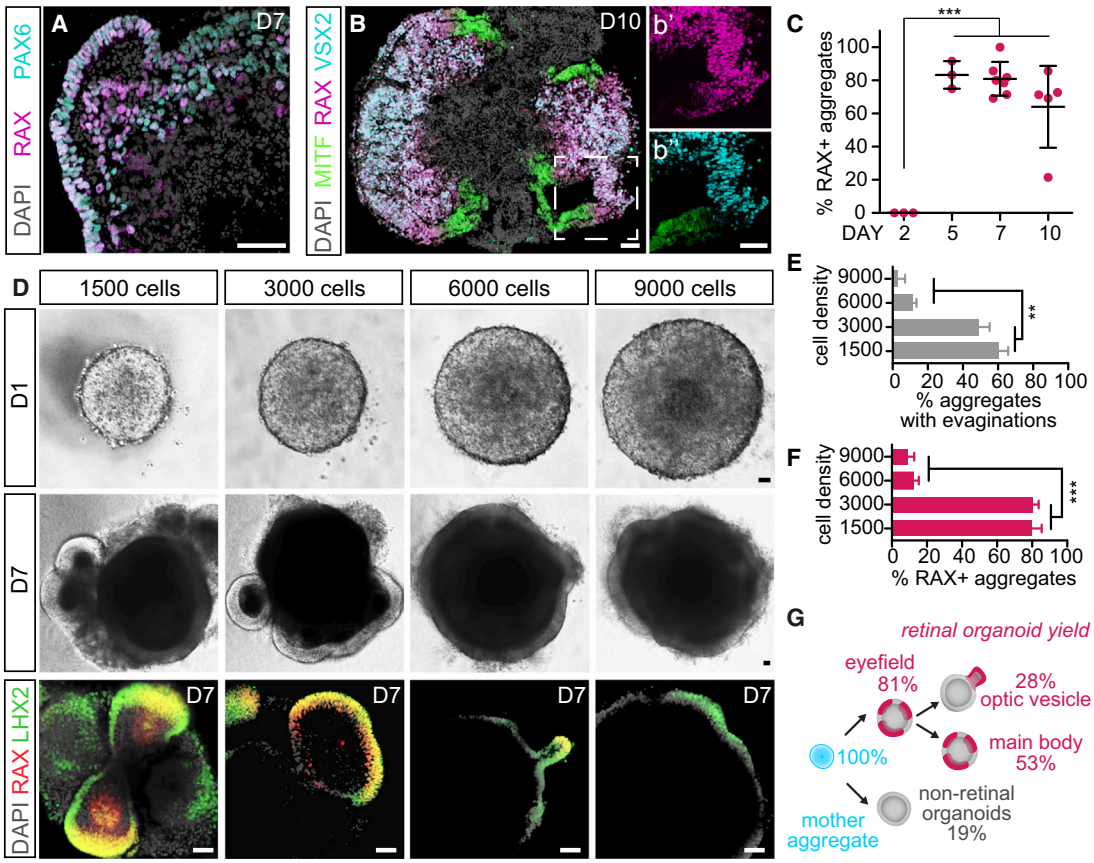

Figure 2. Low Frequency in Potential Optic-Vesicle Formation, but Not Eyefield Induction, Limits Retinal Organoidogenesis Efficiency

(A) RAX and PAX6 co-expression, indicating eyefield identity, was detected at day (D) 7.

(B) At D10, large neural retinal areas (RAX^+ $VSX2^+$) with adjacent RPE areas ($MITF^+$ RAX^- $VSX2^-$) were observed. Dashed square indicates region-of-interest shown at higher magnification: RAX^+ (b′) and $MITF^+VSX2^+$ (b″).

(C) Quantitative analysis of eyefield induction: the number of RAX^+ aggregates increases over time, based on scoring immunostained aggregate sections at D2–10 ($N \geq 3$, $n \geq 10$; 3,000 mESCs seeding density).

(D–F) Eyefield induction efficiency was dependent on cell-seeding density and did not correlate with evaginations (see also Figure S2).

(D) Phase-contrast images and immunostaining images for eyefield transcription factors RAX and LHX2 of aggregates developing from different cell-seeding densities at D1 and D7 as indicated. (E) Quantification of aggregates with evaginations and (F) RAX^+ aggregates, developed from different cell-seeding densities ($N = 4$, $n = 24$).

(G) Scheme of eyefield and optic-vesicle formation efficiency ($N = 7$, $n \geq 10$). mESC-derived starting (mother) aggregates are formed with 100% efficiency, out of which 81% develop eyefields and 28% form optic vesicles. Thus, according to the first protocol, aggregate evagination and optic-vesicle formation limit the efficiency of retinogenesis, and the majority of eyefield-containing tissues are frequently discarded.

n = individual organoids per independent experiment (N). Data shown are means ± SD. $^{**}p < 0.01$, $^{***}p < 0.001$. Scale bars, 50 μm. See also Figure S2.

neurogenic transcription factor ASCL1 (Figures 3A and 3B) suggested a regulated temporal process of organoidogenesis. The number of cells positive for the mitosis marker phosphohistone H3 (PHH3) significantly decreased from D12 to D25 ($N = 3$, $n = 5/N$, $p < 0.0001$). $ASCL1^+$ cells significantly increased from D12 to D16 ($N \geq 3$, $n = 5/N$, $p < 0.0001$) and decreased thereafter, indicating progenitor expansion followed by depletion, similar to retinogenesis in vivo. The vast majority of organoid neuroepithelia express VSX2, the earliest specific marker of retinal progenitors, at D10 (67% ± 8% $VSX2^+$ organoids) versus D7 (7% ± 2% $VSX2^+$ organoids) ($N \geq 5$, $n > 30$ per time point, $p < 0.0001$; Figures 3C and S3A). Photoreceptor-specific marker CRX was expressed in 89% ± 3% of organoids at D15, but not at D12 ($N \geq 3$, $n > 30$ scored per time point, $p < 0.0001$; Figure 3C). ELAVL3/4 (HUC/D), an early marker

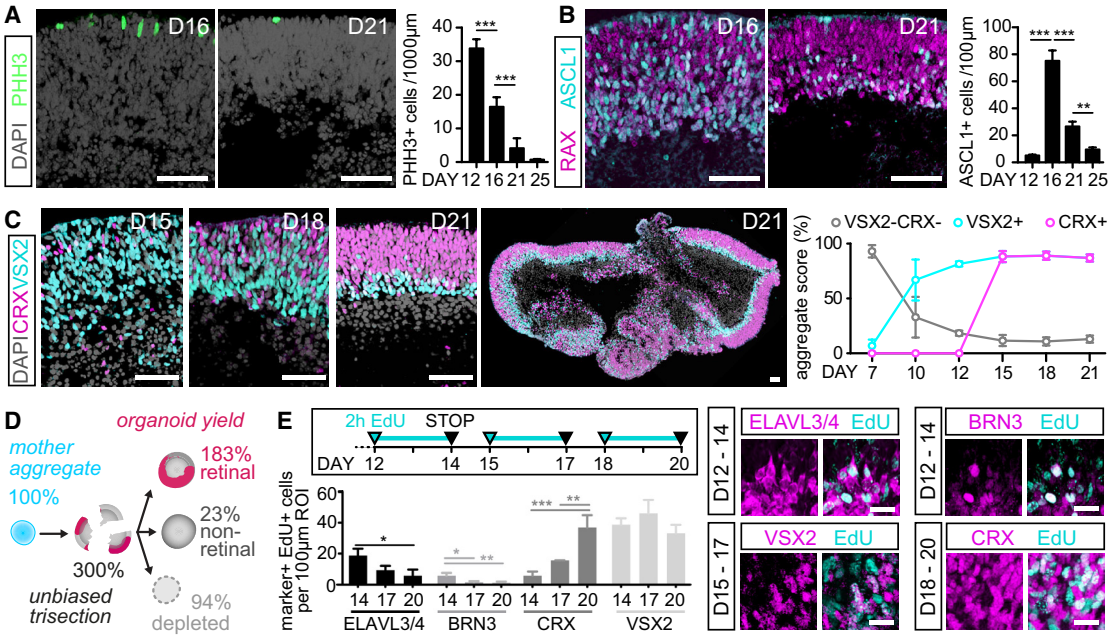

Figure 3. Efficient Retinal Histogenesis from Trisected Day-10 Aggregates

(A and B) Organoid development followed a temporal program, as evidenced by (A) mitotic marker phosphohistone H3 (PHH3) and (B) expression of the neurogenic marker ASCL1 (N = 3, n = 5).

(C) Developing large epithelial structures express markers for retinal progenitors (VSX2) and photoreceptors (CRX), indicating retinal identity. Photoreceptors were localized at the outer (apical) side of the aggregate. VSX2 is also expressed in postmitotic bipolars. Scoring analysis of (retinal) aggregates immunostained for VSX2 and CRX ($N \geq 4$, $n > 20$).

(D) The trisection approach increased the total yield of retinal organoids at D21. Each starting aggregate was trisected at D10 into three evenly sized portions, out of which 183% ± 44% developed into retinal organoids (score of RAX^+ organoid section at D21; N = 4, $n \geq 20$; see Supplemental Experimental Procedures and Table S1), the minority developed as non-retinal organoids (23%), and the remainder degraded by D21.

(E) Cell birthdating showed a defined timing of retinogenesis. The scheme shows 2-hr EdU pulses (open triangle) analyzed after a 2-day chase period (closed triangle). Graphs represent quantitative analysis of birthdated cells (N = 3, n = 3/N). Representative images of birthdated $ELAVL3/4^+$ (amacrine, horizontal, ganglion cells), $BRN3^+$ (ganglion cells), VSX2 (progenitors, bipolar cells), and CRX^+ (photoreceptors) cells.

n = individual organoids per independent experiment (N). Data are represented as means ± SD. *p < 0.05, **p < 0.01, ***p < 0.001. Scale bars, 50 µm (A–C) and 20 µm (E). See also Figure S3.

of ganglion and amacrine cells, was first detected at D10 in most of the RAX^+ regions (Figure S3B), marking the onset of retinal neurogenesis (50% ± 12% $ELAVL3/4^+$ RAX^+ organoids at D10 versus D7, $N \geq 5$, $n \geq 8/N$, $p < 0.0001$), whereas earlier, at D7, ELAVL3/4 was only found in some non-retinal organoid parts (RAX^-). Organoid scoring of immunostained sections revealed that markers of retinal ganglion (BRN3, ELAVL3/4) and amacrine cells (ELAVL3/4, TFAP2A, BHLHB5) were upregulated between D10 and D15, and photoreceptor (CRX, RCVRN, OTX2, RHO), bipolar (OTX2, VSX2), and Müller glia (glutamine synthetase, GLUL) cells by D15–18 (Figures S3B–S3G). Structurally, photoreceptors (CRX^+, $RCVRN^+$) were located on the outer (apical) surface of the organoid, and $PAX6^+$ cells (amacrine and ganglion cells) accumulated toward the organoid center, while VSX2-expressing cells (bipolar cells, Müller glia) were localized in an intermediate layer (Figures 3C and S3E), indicating that retinal organoids by D21 display a stratified architecture comparable with early postnatal retina in vivo. In comparison with previous protocols, the trisection of the starting (mother) aggregate at D10 resulted in a 3-fold increase in organoids that continued to develop. This resulted in twice as many differentiated large stratified retinal organoids at D21 as starting aggregates (183% ± 44%, N = 4, $p < 0.05$, number of RAX^+ retinal organoids scored at D21 compared with number of starting organoids; Figures 3D and S1C–S1E); only a minority were non-retinal (23%). Each D21 retinal organoid contained a major proportion of retinal tissue with a circumference of 1.2 ± 0.4 mm (N = 2, n = 10; Figures S1F and S3E), which is about one-third the size of a postmitotic mouse retina in vivo at postnatal day 10 (Löffler et al., 2015).

Approximately one-third of trisected organoids degraded before D21 by falling apart during media changes or at specimen fixation. Commonly, these organoids had no compact neuroepithelium, suggesting non-retinal phenotypes.

Reproducibility of Retinal Organoidogenesis Indicated by Cell Birthdating, and Comparative Temporal Gene Expression Analysis of Individual Organoids

To investigate the variability of retinal histogenesis among individual organoids and over time, we first conducted 5-ethynyl-2′-deoxyuridine (EdU) pulse-chase birthdating experiments (Figures 3E, S3H, and S3I). EdU was applied for 2 hr at D12, D15, or D18 and EdU-retaining cells were quantified 2 days later (data given as mean ± SD [range] per 100 μm random organoid regions of interest [ROI], N = 3, n = 3/N, 1 ROI/n). We found, on average, a total of 88 ± 20 (49–121) ELAVL3/4$^+$ (amacrine, horizontal, ganglion cells) and 18 ± 5 (4–28) BRN3$^+$ cells (ganglion cells) in developing D14 organoids. Both markers birthdate cell types that appear early in retinogenesis and the majority were also born early in the organoids, before D15 (Figure 3E, D14 versus D20, $p < 0.05$ and $p < 0.01$). The total number of BRN3$^+$ cells significantly increased over time (D20 40 ± 4 [24–58], $p < 0.01$ compared with D14) and ELAVL3/4 cells remained rather constant. The variability of birthdated ELAVL3/4 and BRN3 cells were high at all three time points according to the coefficient of variation (CV) (ratio of SD to mean; mean CV 40% and 59%, respectively). VSX2$^+$ EdU$^+$ cell numbers remained similar at all three time points (mean CV 17%): initially, they most likely represented progenitors and later bipolar cells. In contrast, significantly more CRX$^+$ (photoreceptors) appeared later, at D18 rather than D12 or D15 (D12 versus D18, $p < 0.001$). The total number of CRX$^+$ photoreceptors increased strongly over time (D14, 30 ± 2 [18–39] versus D17, $p < 0.05$, and versus D20, $p < 0.0001$; CRX$^+$ 170 ± 22 [132–219]). The low variability of CRX$^+$ EdU$^+$ cells at D17 (16 ± 0.2 [14–17], CV 1%) suggested robust photoreceptor genesis, but the variability strongly increased at D20 (37 ± 8 [20–54], CV 22%). In conclusion, the total number of BRN3 and CRX cells increased significantly over time, BRN3 and ELAV3/4 cells being born earlier and CRX cells later, indicating temporally regulated and robust retinogenesis. The birthdating data suggest differential variabilities in retina organoidogenesis, and that the variation of total cell numbers at the end of retinal organoidogenesis (D20) is higher than the variation reported in the adult mouse retina in vivo (Jeon et al., 1998).

To determine how synchronous organoids develop and to reveal potential variation at the molecular level, we performed real-time qPCR gene profiling of individual organoids. We collected 12 single organoids at each of five different time points (D7, D10, D15, D18, and D21; 60 organoids in total) and analyzed the expression of 21 genes in each organoid (normalized to *Actb*; Figures 4 and S4, Tables S2 and S3). We detected significant changes in genes associated with developing and mature retinal cells, including progenitors (proneural and stemness genes), ganglion cells, interneurons, photoreceptors, and Müller glia. Temporal gene-expression profiles indicated an early and late phase of organoidogenesis (see dashed vertical lines in Figure 4A). For example, there was a large and stable increase in *Crx*, the earliest known regulator of photoreceptor genesis, from D10 to D21 ($p < 0.00001$), whereas *Rcvrn*, indicating mature photoreceptors, increased later, at D18 ($p < 0.00001$ compared with D7). Hierarchical clustering (Figure 4B) revealed groups of genes increasing significantly before D15, indicating functions in early retinogenesis (clusters I, II, and V), such as those related to ganglion cell genesis (*Atoh7*, *Isl1*, and *Brn3*). In contrast, genes regulating late retinogenesis, such as *Nrl* (earliest known marker of postmitotic photoreceptors) and *Rlbp1* (Müller glia), became upregulated after D15 (clusters VI–VII). Many genes changed continuously (interneuron related, such as *Foxn4*, *Meis2*, *Neurod1/6*) and a few underwent smaller changes (such as *Rax*, *Pax6*, *Sox9*, *Vsx2*, mostly progenitor related). Low levels of *Mitf* suggested limited RPE cell fate.

The CV for each gene was used to capture relative variability in interindividual organoid gene expression (Mason et al., 2014) (CV include data with $\Delta\Delta$Cq values $\geq \pm 1.0$; Table S3). For example, neurogenic transcription factor *Ascl1* increased 120-fold up to D21, with a low mean variability (D10–21 mean CV 15%), indicating effective neurogenesis. *Crx* expression had a relatively low variability in the main phase of organoidogenesis (CV 12% at D15 and D18), suggesting robust photoreceptor production. However, *Crx* became more variable at D21 (CV 51%), and *Rcvrn*, indicative of further differentiated photoreceptors, was also quite variable at D18–21 (mean CV 26%). Given that retinal cell genesis is completed at D21 (Figure 3A), the observed variability might be due to processes such as ongoing cell maturation. The molecular data matched those for related proteins well (Figures 3 and S3). Photoreceptor birthdating indicated less variability during the main phase compared with the end of retinogenesis, and RCVRN protein was more heterogeneously expressed than CRX throughout a given organoid at D21 (Figures 3E, S3E, S3H, and S3I). In contrast, although ganglion and amacrine cell birthdating showed interorganoid variation throughout retinogenesis, expression of related genes (D10–18 mean CV of *Atoh7*, *Brn3b*, and *Foxn4* 14%) was less variable during neurogenesis, but stronger at the end of retinogenesis (D21 mean CV 41%). The average CV for all 21 genes at D10–21 was 35%. Overall, most genes analyzed show reproducible

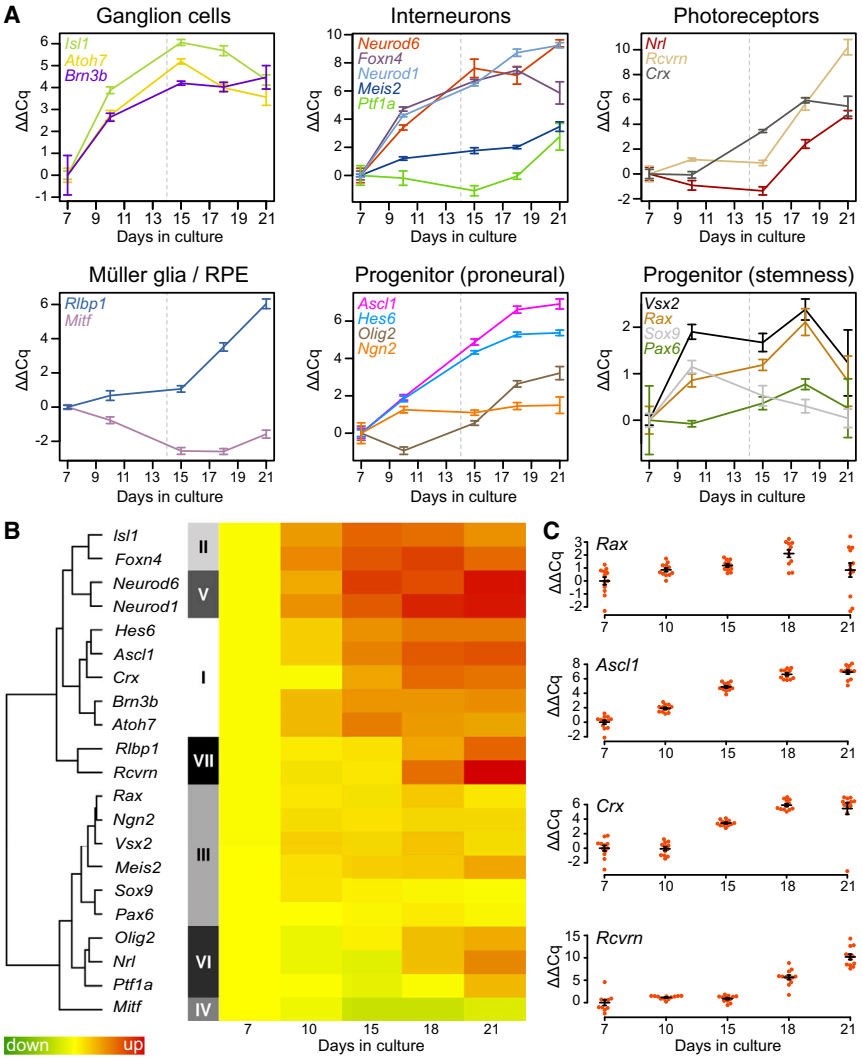

Figure 4. Temporal Gene Expression Comparison of Multiple Individual Organoids Indicated Reproducible mESC-Derived Retinogenesis

(A) Real-time qPCR analysis of retinal differentiation genes in individual organoids during organoidogenesis. At each of five different time points (days [D]), 12 single organoids were randomly sampled and analyzed individually for 21 genes (normalized to *Actb*). Average expression values (line graphs) for each gene were further normalized to D7 (ΔΔCq method) to yield relative expression values (log2 scale). Vertical dashed lines facilitate visualization of gene-expression changes before and after D15, which potentially correspond to early and late retinogenesis.

(B) Heatmap of gene-expression data shown in (A). Hierarchical clustering based on the Euclidean distance between genes (yellow-red scale corresponds to the lowest to highest value for each gene and reveals clusters I–VII).

(C) Scatterplots show gene expression of individual organoids (red dots) and thereby provide insight into interorganoid variability. Per time point, n = 12 individual organoids (n = 60 total) within one independent experiment (N).

Data are represented as means ± SEM. See also Figure S4; Tables S2 and S3.

expression across individual organoids at a given time point, and comparable temporal changes supporting an effective onset and progression of retinal histogenesis in the organoid system. However, our results also revealed differential levels of molecular and phenotypic organoid heterogeneity, suggesting that various processes, such as cell maturation, ontogenetic cell death, and contribution of non-retinal organoid tissue, might be origins of variation. Knowing these variability sources will likely facilitate further improvements in organoidogenesis and downstream applications.

Notch Signaling Inhibition Revealed Time-Dependent Progenitor Competence in mESC-Derived Retinal Organoidogenesis and Enabled the Generation of Cone- or Rod-Enriched Organoids

Based on the observed sequence of genes expressed and cells synchronously generated, we hypothesized that the trisection method facilitates reproducible experiments to differentially stimulate the generation of retinal cell types that appear early and late. Thus, we performed timed application of the Notch inhibitor DAPT (Figures 5 and S5), which is widely used to force differentiation and has been applied in late retinal organoidogenesis (Eiraku et al., 2011). We observed that early DAPT treatment (D12–14, Figures 5A and 5B) significantly increased the number of cone photoreceptors indicated by counts of TRBETA2$^+$ (226-fold, $p < 0.0001$) and S-OPSIN$^+$ cells (42-fold, $p < 0.001$) compared with control (N = 3, n = 5). The number of cells expressing OTX2, a homeodomain transcription factor expressed in early and mature photoreceptors and bipolars, was no higher than in the control. However, after early DAPT treatment the majority of OTX2$^+$ cells co-expressed SALL3, a known regulator of cone genesis. After late DAPT treatment (D16–18, Figures 5C, 5D, and S5A–S5C) the total numbers of rod

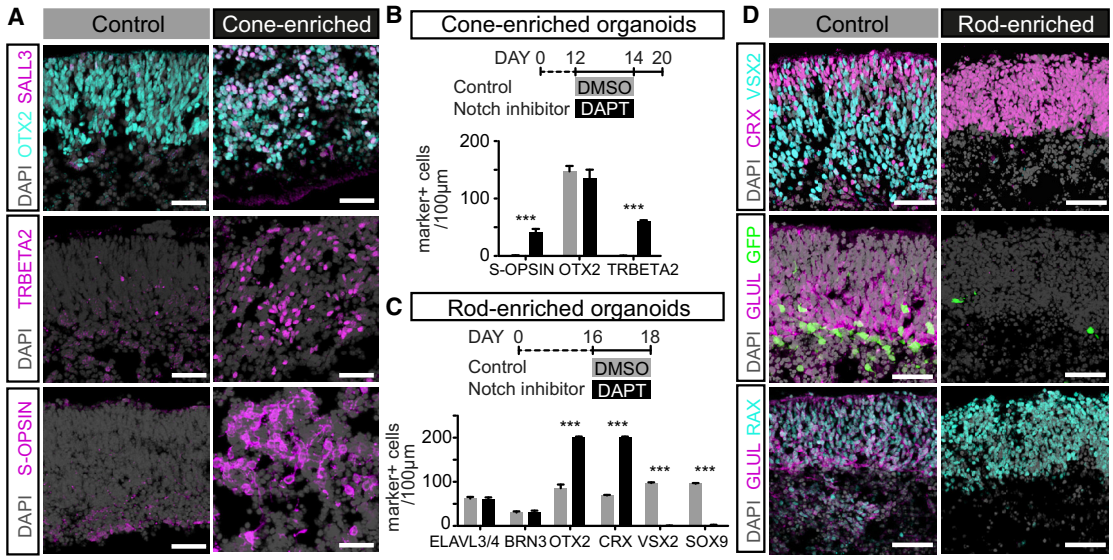

Figure 5. Generation of Rod- or Cone-Photoreceptor-Enriched Organoids by Timed Inhibition of Notch Signaling

(A and B) Notch inhibition by DAPT at early time points (D12–14) increased the number of cone photoreceptors. (A) Images of immunostained organoid sections and (B) graphs with quantification of cone marker expressing cells (TRBETA2$^+$, S-OPSIN$^+$) in DAPT-treated and control (DMSO) organoids (N = 3, n = 5).

(C and D) Notch inhibition at later time points (D16–18) resulted in rod-enriched organoids. (C) Quantification and (D) images of cell-type-specific markers (BRN3$^+$, ganglion cells; CRX$^+$, photoreceptors; ELAVL3/4$^+$, ganglion, amacrine, horizontal cells; GLUL$^+$, Müller glia; VSX2$^+$, progenitors, bipolars) in DAPT-treated and control (DMSO) organoids (N = 3, n = 5). hPAX6GFP-expressing cells were greatly reduced by Notch inhibition. Top panels of (B) and (C) show schemes of the experimental paradigms.

n = individual organoids per independent experiment (N). ***p < 0.001. Scale bars, 50 µm. Data are represented as means ± SD. See also Figure S5.

photoreceptors (CRX$^+$ and RCVRN$^+$) were strongly increased, whereas progenitors (VSX2$^+$, KI67$^+$, PAX6$^+$, hPAX6GFP$^+$), Müller glia (GLUL$^+$, SOX9$^+$), and bipolars (VSX2$^+$, PRKCA$^+$, VSX1$^+$) were almost completely absent after DAPT treatment (not all shown), suggesting that Notch inhibition prevented their fates. The numbers of ganglion and amacrine cells (ELAVL3/4$^+$) were not significantly affected. DAPT applied at D14–16 (Figure S5D) led to a less pronounced increase in photoreceptors at D18, compared with when it was applied at D16–18. Our results suggest that progenitors change their neurogenic competence throughout organoidogenesis, so that by tuning Notch signaling at defined time points it is possible to alter the proportions of retinal cells, specifically increasing cone or rod photoreceptors in correlation with early and late stages of retinal development, respectively.

hPAX6GFP Labeled Retinal Progenitors and Subtypes of Inner Neurons in mESC- and hESC-Derived Retinal Organoids

To further refine our understanding of the course of retinogenesis in the organoid system, we studied hPAX6GFP reporter expression (Figures 6 and S6). hPAX6GFP was first detected with lower fluorescent signal intensity by D10 in the neuroblast layer of organoids derived from mESC clone 1 (Figure 1B). The GFP cell numbers increased until D18 and decreased from D18 to D21. By D21, GFP$^+$ cells had accumulated in the inner nuclear layer (INL)-like region of the organoid, starting to extend processes to an inner plexiform layer (IPL)-like region (Figure 6A). Clone 1 was analyzed in more detail (Figures 6A and S6A), because GFP expression in clone 2 was rather sparse and appeared much later (Figure S6B). GFP$^+$ cells at D15–18 showed co-expression of PAX6 and RAX, SOX9, and VSX2, as well as the proliferation markers PHH3 and MCM6, suggesting retinal progenitor identity (Figures 6A and S6A). Not all PAX6$^+$ cells expressed GFP, which could be due to the species difference (mouse/human) or the lack of enhancer elements in the BAC. With ongoing progenitor depletion, more GFP$^+$ cells accumulated in the INL-like region, suggesting genesis of a subset of retinal interneurons. Indeed, the majority of GFP$^+$ cells at D21 expressed the pan-amacrine marker TFAP2A (Figure 6A). Subsets of GFP$^+$ cells immunostained for bHLHB5 (GABAergic amacrines) and co-expressed EBF3 (glycinergic amacrines) and CALB2, indicating that a broad range of amacrine subtypes can be formed in retinal organoids (Figures 6A and S6A;

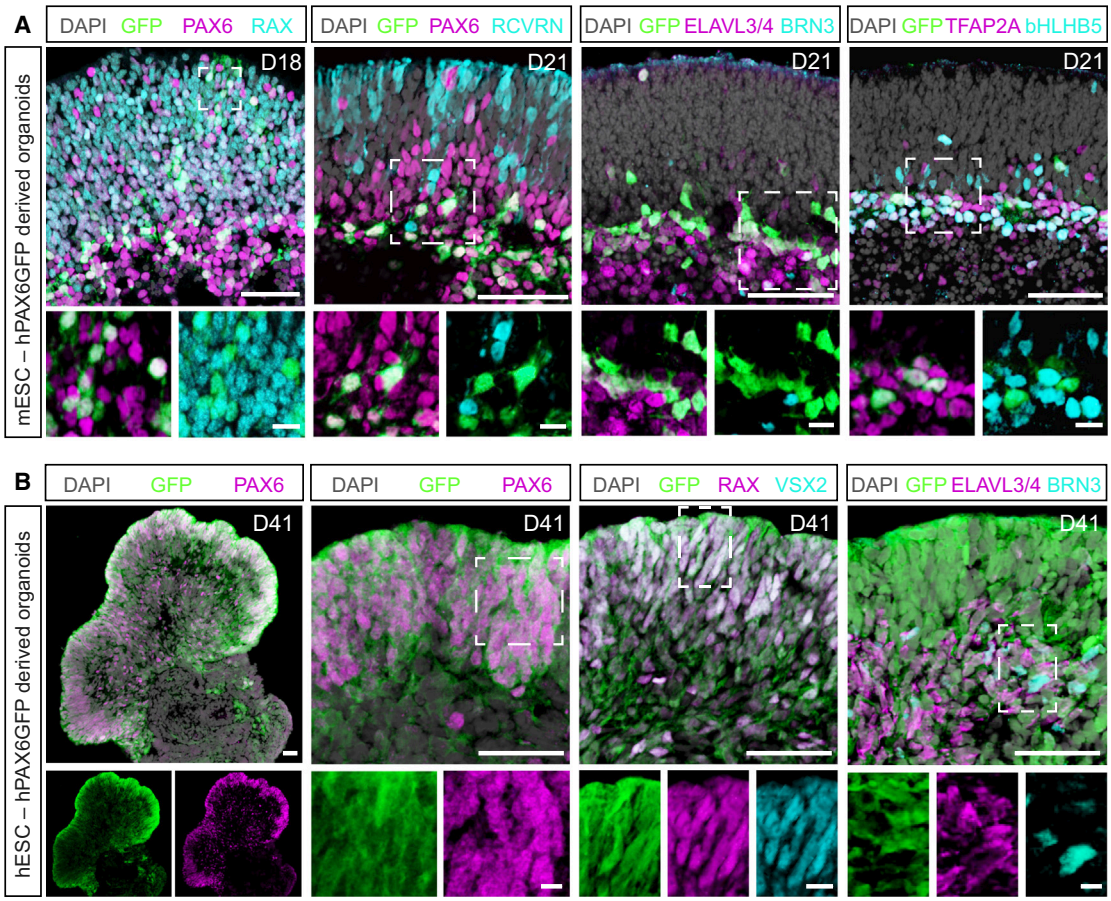

Figure 6. hPAX6GFP in mESC- and hESC-Derived Retinal Organoids

(A and B) Analysis of transgenic hPAX6GFP expression in (A) mESC-derived and (B) hESC-derived retinal organoids. (A) At day (D) 18, weakly GFP$^+$ cells in the neuroblastic layer co-expressed the retinal progenitor markers RAX and PAX6. At D21, GFP$^+$ cells had accumulated in the inner nuclear layer (INL)-like region and co-localized with ELAVL3/4 and PAX6, indicating amacrine and horizontal cells. GFP$^+$ cells are not co-labeled with photoreceptor, bipolar (OTX2, RCVRN), or ganglion cell (BRN3$^+$) markers. GFP$^+$ cells co-expressed the pan-amacrine marker TFAP2a and bHLHB5, expressed by GABAergic amacrines. (B) Overview and ROI images of immunostained human organoid sections at D41: GFP was detected in PAX6$^+$, RAX$^+$, VSX2$^+$, and ELAVL3/4$^+$ cells. Just as in mouse organoids (A), ganglion cells (BRN3) were mostly GFP negative.

Scale bars represent 50 μm, and 10 μm for high magnifications shown in (A) and (B). See also Figure S6.

Table S1). At D21, GFP$^+$ cells expressed PAX6, and did not co-localize with photoreceptor or bipolar markers (CRX, RCVRN, OTX2). The GFP$^+$ progeny contained amacrine and horizontal cells (ELAVL3/4), but no retinal ganglion cells (BRN3) or Müller glia (GLUL). We also positively probed hPAX6GFP reporter expression in CNS regions outside the retina in mESC-derived cerebral organoids (Figure S6C; Eiraku and Sasai, 2011). We sought to provide initial evidence for hPAX6GFP expression in human retinal organoids derived from two previously reported hESC lines (Rostovskaya et al., 2012) by adapting a previously published protocol (Nakano et al., 2012). Comparable with our trisection approach in the mESC system, we manually dissected each individual human organoid into three to five evenly sized tissue parts on D18 after aggregation. In D41 organoids, GFP was detected in regions with neuroepithelial structure in two different hESC reporter lines, which co-labeled with PAX6, RAX, and VSX2: these indicated the identity of the retinal progenitors (Figure 6B; N = 4; line 2 not shown). Comparable with previous reports, we observed the first ELAVL3/4$^+$ (amacrine and horizontal cells) and BRN3$^+$ (ganglion cells) cells in D41 hESC-derived retinal organoids in line 1, but not line 2 (not shown). Thus, just as in mouse retinal organoids (Figure 6A), human ganglion cells (BRN3$^+$) were mostly GFP$^-$ (Figure 6B), while GFP labeled mouse and human progenitor (RAX$^+$, PAX6$^+$) and amacrine cells (ELAVL3/4$^+$).

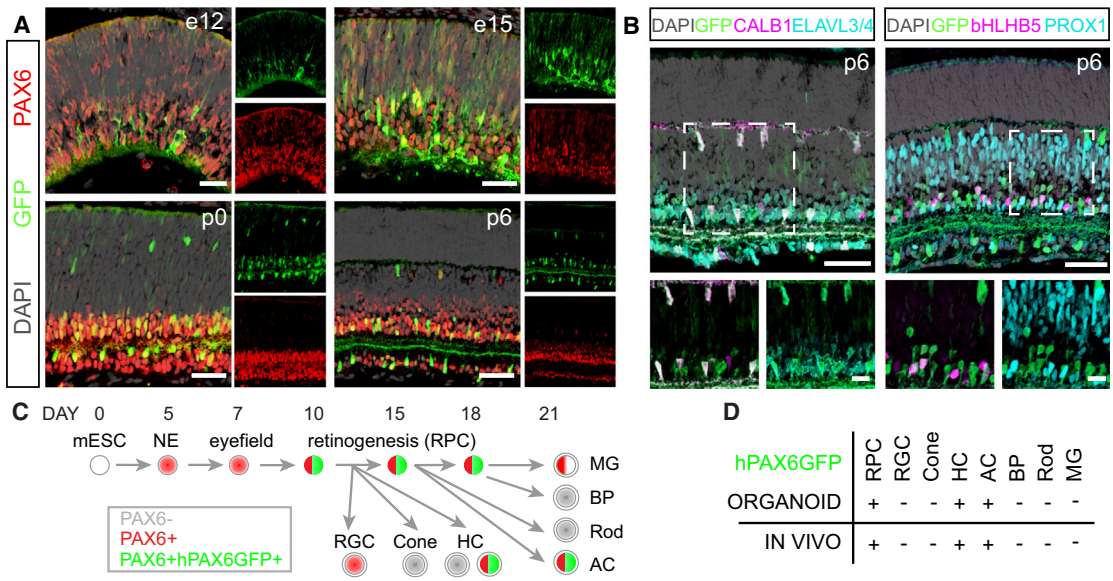

Figure 7. Characterization of Transgenic hPAX6GFP Expression in the Developing and Mature Mouse Retina

(A) Images of GFP and PAX6 immunostained hPAX6GFP reporter mice retina sections at embryonic days (e) 12 and 15, and postnatal days (p) 0 and 6 show GFP in progenitors and subsets of PAX6$^+$ postmitotic horizontal and amacrine neurons.

(B) Similar to the retinal organoids, GFP$^+$ cells in the mouse retina also co-expressed the markers CALB1 (amacrine, horizontal cells) and ELAVL3/4 (amacrine, horizontal, ganglion cells), but not the ganglion cell marker BRN3. Subsets of GFP$^+$ cells also co-expressed PROX1 and bHLHB5 (amacrines).

(C and D) Summary scheme (C) and comparison table (D) show that transgenic hPAX6GFP expression showed similar retinal cell types in the retinal organoid system and mouse retina in vivo. GFP expressed (+)/not expressed (−); RPC, retinal progenitor cell; RGC, retinal ganglion cell; HC, horizontal cell; AC, amacrine cell; BP, bipolar cell; MG, Müller glia; NE, neuroepithelium.

Scale bars represent 50 μm, and 10 μm for high magnifications shown in (B). See also Figures 6, S6, and S7.

Comparative hPAX6GFP Expression Analysis in Retinal Organoids and Mouse Retina In Vivo Revealed Similar Expression Patterns and Timing

We sought to gain further insights into organoidogenesis by comparative analysis of retinal organoids derived from the hPAX6GFP transgenic reporter mESC line (Figures 6 and S6) and the respective transgenic mouse strains (Figures 7 and S7). We generated transgenic mice carrying the same hPAX6GFP reporter as the mESC. GFP was first detected by embryonic day 12 (e12) in the retina in vivo (Figure 7A), when neurogenesis starts. Most GFP$^+$ cells co-expressed PAX6 and various progenitor markers matching our organoid data. By postnatal day 0 (p0), GFP$^+$ progenitors had become more restricted to the central retina (Figures 7A and S7A). By p0–6, GFP was detected in the developing INL and ganglion cell layer (GCL), and by p11 (the end of retinogenesis) and in adults it was also detected in the horizontal cell layer (Figures 7A, 7B, and S7A–S7C). GFP$^+$ cells were evenly distributed in the central and peripheral developing and postmitotic retina (see retina section and flat-mount data, Figures S7A and S7B), but not in the RPE or lens, both of which expressed PAX6 (data not shown). By p6–11, GFP$^+$ cells co-expressed the amacrine and horizontal cell markers CALB1, ELAVL3/4, and PROX1, and the amacrine markers bHLHB5 and SOX2 (Figures 7B and S7D). In line with our results in mouse and human retinal organoids, hPAX6GFP did not co-localize with retinal ganglion cells in vivo (Figure S7D). GFP was not expressed in Müller glia in vivo but was expressed in mouse retinal explant culture, suggesting upregulation of hPAX6GFP in reactive glia (Figure S7E). These comparative analyses reveal that hPAX6GFP is similarly expressed in transgenic mice in vivo and in the mESC- and hESC-derived retinal organoids in a subset of developing retinal progenitors, in amacrine and horizontal cells (Figures 7C and 7D).

DISCUSSION

We developed an efficient approach for retinal organoidogenesis stemming from the pioneering protocol (Eiraku et al., 2011) which makes use of the power of PSC to generate self-organized, complex, stratified 3D retinal tissue. The original protocol utilizes the generation of OC-like structures, but requires the OV-like evagination of the neuroepithelium and its manual dissection. We observed

that about 80% of organoid neuroepithelia developed into eyefields, comparable with previous publications (Table S1). However, using E14TG2a mESC, or the original reported RAX-GFP mESC line (kindly provided by Y. Sasai, Japan [Eiraku et al., 2011]), others (Hiler et al., 2015) and our group (RAX-GFP data not shown) observed that OV-like structures form irregularly and OC-like structures infrequently. The fact that evagination of the eyefield neuroepithelium occurs rather inefficiently in about 20% of aggregates, and varies between PSC lines (Hiler et al., 2015; see also Figure 2G and Table S1), which might depend on the intrinsic capacity of the PSC line or on culture conditions, currently limits retinal organoidogenesis. Notably, eyefield domains achieved with E14TG2a mESCs are rather large (covering up to 50% of the organoid at D10). OV size has been reported to be a critical factor influencing OC formation (Decembrini et al., 2014; Eiraku et al., 2011), suggesting that this may be a major factor preventing OC formation. Thus, factors affecting eyefield restriction and expansion, such as sonic hedgehog, may be differentially regulated in different mESC lines. By merely isolating the aggregate evaginations, the majority of eyefield tissues were discarded. Furthermore, our data show that evaginations frequently lack eyefields, and are thus not reliable predictors of prospective retinas. By trisecting an unbiased simple organoid neuroepithelia, we overcame these limitations. The trisection protocol utilizes all starting aggregates to improve the retinal organoid yield and enables robust generation of large, stratified 3D retinal organoids derived from wild-type mESC.

Our data show that the trisection approach results in the generation of retinal organoids with a cell birth order and developmental timing comparable with mice in vivo. Expression of bHLHB5 (GABAergic amacrines) and EBF3 (largely glycinergic amacrines) in different subsets of amacrine cells at D21 also show not only that the major retinal cell types differentiate in mouse retinal organoids but also that subtype specification is induced. To gain further understanding of the reproducibility of retinal organoidogenesis, we performed cell birthdating experiments and analyzed interindividual organoid variation in gene-expression levels. The molecular data were consistent with the immunostaining-based phenotypic results, showing significant differences in the types of cells born earlier (ganglion cells) and later (photoreceptors), as well as in related gene-expression changes. Overall, the data indicate a robust onset, temporal order, and progression of retinal histogenesis; this suggests that regulated developmental programs are repeated. However, comparing individual organoids also revealed differential gene-expression variability. Although some genes are expressed quite robustly, others are more variable at the onset, end, or even throughout retinal organoidogenesis. Many of the genes investigated have functions not only in the developing but also in the maturing and adult retina. Whether the observed gene-expression variability is the cause of the phenotypic heterogeneity of the organoids at the protein level, or whether they are consequences of other processes (e.g., ontogenetic cell death and cell maturation) remains unknown. Future studies of the origins and consequences of gene-expression variation in retinal development are needed to refine our understanding of the relationships between phenotypic and molecular heterogeneity in retinal organoidogenesis and animals in vivo.

Comparative analysis of transgenic hPAX6GFP expression revealed similarities between the retinal organoid system and the mouse retina in vivo. Our analyses indicated a similar sequence of hPAX6GFP$^+$ retinal cell types in mice in vivo, and in mESC- and hESC-derived retinal organoids: progenitors and retinal interneurons (horizontal and amacrine cells). This was despite differences in the number of hPAX6GFP$^+$ cells. In early postmitotic mouse retinal organoids hPAX6GFP$^+$ cells participated in the formation of an IPL-like region, indicating that important features of the ultimately highly complex inner architecture of the mature retina are generated. The two mESC lines analyzed expressed GFP differentially, possibly due to different insertion sites. The hPAX6GFP transgene does not contain all its enhancers, and carries the GFP-containing cassette in exon 4 (Figure S1), disrupting gene function, so that the observed GFP pattern may also indicate cell heterogeneity. This might be of significance, since the functional importance of spatiotemporal levels of PAX6 expression during development is well established (Shaham et al., 2012). Our results suggest that the hPAX6GFP transgenic reporter in the human and mouse ESC organoid system might be a useful tool for studying progenitor lineages, neuronal differentiation, maturation, survival, stratification, and neural wiring in retinal and brain organoids. Moreover, the organoid system might offer a faster way to identify robust and reliable reporter expression in the tissue of interest, prior to the generation of transgenic mice.

For current and future applications of the 3D retinal organoid system, the neuroepithelium trisection approach provides significant advantages in comparison with the mESC protocols currently available (Table S1 and Figures S1C–S1E) and, as indicated by our experiments with the hPAX6GFP hESC, potentially also for human PSCs. First, this approach does not require any transgenic reporter and does not involve the formation of complex evaginations or eyecups, processes reported to be inefficient in all of the published protocols. Therefore, it provides full flexibility for the application of any, and multiple, fluorescent reporters for retinal-organoid-based research. Second, our protocol yields about twice as many retinal organoids as starting aggregates, and retina sizes are comparable with, or even bigger than, those reported previously. Hiler et al.

(2015) recently reported that, following the evagination isolation protocol, the frequency of retinal organoids derived per starting aggregate is about 46% for the RAX-GFP mESC line: our protocol yields 183%. Third, organoids grown with this protocol develop stratified neural retinal tissue, with defined outer nuclear layer, inner nuclear layer, and GCLs, although at the final time point (D21) the inner and outer plexiform layers had not completely formed. Fourth, previous adaptions (Decembrini et al., 2014; Gonzalez-Cordero et al., 2013) of the original 3D retinal organoid protocol have made reporter and OC formation independent by omitting the manual dissection/selection step and, instead, maintaining and maturing the retinal domain inside the mother aggregate. This approach even allows the protocol to be automated. Although photoreceptors develop well inside the mother aggregate, inner retinal cell types and layers either differentiate less well or degenerate more. This may be an advantage for studies focusing on photoreceptors and requiring high numbers of them. However, it might be inconvenient for studies that require the complete retinal structure. Additional modifications, such as maintaining the organoid in Matrigel for two additional days (Decembrini et al., 2014; Gonzalez-Cordero et al., 2013), which restricts its expansion, might be necessary to develop a 3D retina. Our trisection protocol also reduced the size of the organoid at this temporal stage, and likely facilitates further development by, e.g., increasing access for nutrients and oxygen and allowing for better expansion by removing restrictive neighboring tissue. This might also increase the survival of organoids in long-term culture—specifically in the human retinal organoid system—and potentially also for organoidogenesis of other types of tissue. Fifth, timed drug-based Notch inhibition enables forced differentiation of early and late retinal cell types in the organoid system, indicating that neurogenic competence is regulated in a similar way to retina in vivo (Cepko, 2014). Thus, our data suggest a reliable approach for generating large numbers of cone photoreceptors, which are of interest for various applications such as cell replacement therapy.

Therefore, one of our future endeavors will be to apply and optimize the trisection protocol to the human retinal organoid system, and to perform research on human neuronal development, disease modeling, tissue repair, regeneration, and therapies in translational medicine.

EXPERIMENTAL PROCEDURES

Generation of hPAX6GFP mESCs and Reporter Mouse

The eGFP-IRES-puro-pA-FRT-PGK-neo-pA-FRT cassette was inserted directly after the initiating methionine (ATG) in exon 4 of the *hPAX6* gene in the BAC RP11-26B16, followed by the insertion of piggyBac inverted repeats by recombineering, as previously described (Rostovskaya et al., 2012; Figure S1A). The BAC was co-transfected with hyPBase expression vector to mESC; blasticidin-resistant clones were screened by PCR for transposition signature, and phenotyped using pluripotency markers (Figure S1B). Generation of transgenic mice was performed as previously described (Rostovskaya et al., 2013). Animal licenses were obtained according to the TU Dresden and German Federal regulations. See Supplemental Experimental Procedures.

mESC Culture

E14TG2a (MMRRC, UC Davis) wild-type and hPAX6GFP transgenic mESCs were cultured in mESC medium supplemented with 10^3 U/ml leukemia inhibitory factor and 1 μM PD0325901. Cells were passaged every 2–3 days using TrypLE Express (Invitrogen).

mESC Retinal Organoidogenesis

Retinal differentiation was adapted from a previously reported protocol (Eiraku et al., 2011). In brief, mESC aggregation in 96-well plates was defined as day 0 (D0), and 2% Matrigel was added on D1. After being cultured (20% O_2) until D7, the organoids were transferred to bacterial-grade petri dishes for further culture in retinal maturation medium 1 (40% O_2). On D10, the organoids were manually trisected using surgical tweezers (Fine Science Tools, Dumont No. 5) and further cultured in retinal maturation medium 2. EC23 (0.3 μM) was added from D10 to D14. See Supplemental Experimental Procedures.

hESC Retinal Organoidogenesis

Retinal differentiation of H7.S6 PAX6GFP BAC transgenic hESC was performed by adapting a previously reported protocol (Nakano et al., 2012). Permission to work with hESCs was granted by the Robert Koch Institute, Berlin, Germany. See Supplemental Experimental Procedures.

Tissue Preparation and Immunohistochemistry

Samples were fixed in 4% paraformaldehyde, and cryoprotected (30% sucrose, overnight) and embedded in tissue-freezing medium (Jung). Frozen sections were cut at 12–20 μm. Immunostaining was performed using standard protocols. See Supplemental Experimental Procedures.

Single-Organoid qPCR

RNA from single retinal organoids (n = 12 randomly selected individual organoids per time point) were isolated and reverse transcribed using a Power SYBR Green Cells-to-Ct kit (Ambion). Gene-specific primers were designed using Primer3 (Simgene.com) software, spanning an exon-exon junction where applicable. Real-time qPCR reactions were performed with SsoFast EvaGreen Supermix (Bio-Rad) according to the manufacturer's instructions (C1000, CFX96, Bio-Rad). See Supplemental Experimental Procedures.

Data Analysis

Samples were imaged on a Zeiss ApoTome2, LSM Confocal, or Spinning Disc Confocal microscope. For aggregate scoring, analysis of each aggregate was performed by assessing marker expression on

multiple consecutive sections (>8) on at least two slides (N ≥ 4 independent experiments, n > 10 aggregates/N). For cell counting and co-localization analysis, random ROIs 100 μm wide were used. The x axis of each ROI was positioned radially to the organoid center, with the y axis aligned perpendicular to the organoid surface. ROI images are z axis projections of 5 × 1 μm acquired in Apotome mode using a 20× Plan-Apochromate objective. Cells were counted on 3D reconstructed images using ZEN blue (Zeiss). Organoid circumference and retinal length were measured using the length tool in ZEN blue (Zeiss). Statistical analysis was performed with GraphPad Prism using one-way ANOVA (Tukey's post hoc test) or Student's unpaired t test. Results were considered significant for $p < 0.05$ and data were plotted as mean ± SD if not noted otherwise. See Supplemental Experimental Procedures.

SUPPLEMENTAL INFORMATION

Supplemental Information includes Supplemental Experimental Procedures, seven figures, and three tables and can be found with this article online at http://dx.doi.org/10.1016/j.stemcr.2016.03.001.

AUTHOR CONTRIBUTIONS

M.V., V.B., and M.K. designed the experiments. M.V. and M.K. wrote the paper. M.R. and K.A. generated hPAX6GFP transgenic mESC and mice. M.V. and M.Z. performed the experiments. M.V., M.Z., R.O., and M.K. analyzed the data.

ACKNOWLEDGMENTS

We thank Y. Sasai (RIKEN, Japan) for the RAX-GFP mESC line, M. Wegner (University of Erlangen, Germany) for SOX9, E. Tanaka (CRTD, Germany) for RAX and CRX, and D. Forrest (NIDDK, USA) for TRβ2 antibodies. We thank J. Brzezinski (University of Colorado Denver), S. Oakeley (Basel, Switzerland), G. Kempermann (DZNE), M. Ader, F. Calegari, N. Ninov, and E. Tanaka (all CRTD) for helpful comments on the manuscript. We thank M. Obst, the light microscopy facility, and the animal facility for excellent support. This work was kindly supported by the Funding Programs for DZNE Helmholtz (M.K.), TU Dresden CRTD (M.K.), DFG (KA2794/3-1; SPP1738) (M.K.), MedDrive TU Dresden UKD-Medical Faculty (M.K.), research award Novartis Pharma GmbH (M.K.), Volkswagen Foundation Freigeist fellowship (V.B.), and the European Union's sixth Framework Program ESTOOLS (K.A.).

Received: May 22, 2015
Revised: March 2, 2016
Accepted: March 3, 2016
Published: March 31, 2016

REFERENCES

Boucherie, C., Mukherjee, S., Henckaerts, E., Thrasher, A.J., Sowden, J.C., and Ali, R.R. (2013). Brief report: self-organizing neuroepithelium from human pluripotent stem cells facilitates derivation of photoreceptors. Stem Cells *31*, 408–414.

Busskamp, V., Krol, J., Nelidova, D., Daum, J., Szikra, T., Tsuda, B., Jüttner, J., Farrow, K., Scherf, B.G., Alvarez, C.P., et al. (2014). miRNAs 182 and 183 are necessary to maintain adult cone photoreceptor outer segments and visual function. Neuron *83*, 586–600.

Cepko, C. (2014). Intrinsically different retinal progenitor cells produce specific types of progeny. Nat. Rev. Neurosci. *15*, 615–627.

Decembrini, S., Koch, U., Radtke, F., Moulin, A., and Arsenijevic, Y. (2014). Derivation of traceable and transplantable photoreceptors from mouse embryonic stem cells. Stem Cell Rep. *2*, 853–865.

Eiraku, M., and Sasai, Y. (2011). Mouse embryonic stem cell culture for generation of three-dimensional retinal and cortical tissues. Nat. Protoc. *7*, 69–79.

Eiraku, M., Takata, N., Ishibashi, H., Kawada, M., Sakakura, E., Okuda, S., Sekiguchi, K., Adachi, T., and Sasai, Y. (2011). Self-organizing optic-cup morphogenesis in three-dimensional culture. Nature *472*, 51–56.

Gonzalez-Cordero, A., West, E.L., Pearson, R.A., Duran, Y., Carvalho, L.S., Chu, C.J., Naeem, A., Blackford, S.J., Georgiadis, A., Lakowski, J., et al. (2013). Photoreceptor precursors derived from three-dimensional embryonic stem cell cultures integrate and mature within adult degenerate retina. Nat. Biotechnol. *31*, 741–747.

Hiler, D., Chen, X., Hazen, J., Kupriyanov, S., Carroll, P.A., Qu, C., Xu, B., Johnson, D., Griffiths, L., Frase, S., et al. (2015). Quantification of retinogenesis in 3D cultures reveals epigenetic memory and higher efficiency in iPSCs derived from rod photoreceptors. Cell Stem Cell *17*, 101–115.

Jeon, C.J., Strettoi, E., and Masland, R.H. (1998). The major cell populations of the mouse retina. J. Neurosci. *18*, 8936–8946.

Lamba, D.A., Karl, M.O., Ware, C.B., and Reh, T.A. (2006). Efficient generation of retinal progenitor cells from human embryonic stem cells. Proc. Natl. Acad. Sci. USA *103*, 12769–12774.

La Torre, A., Hoshino, A., Cavanaugh, C., Ware, C.B., and Reh, T.A. (2015). The GIPC1-Akt1 pathway is required for the specification of the eye field in mouse embryonic stem cells. Stem Cells *33*, 2674–2685.

Löffler, K., Schäfer, P., Völkner, M., Holdt, T., and Karl, M.O. (2015). Age-dependent Müller glia neurogenic competence in the mouse retina. Glia *63*, 1809–1824.

Mason, E.A., Mar, J.C., Laslett, A.L., Pera, M.F., Quackenbush, J., Wolvetang, E., and Wells, C.A. (2014). Gene expression variability as a unifying element of the pluripotency network. Stem Cell Rep. *3*, 365–377.

Nakano, T., Ando, S., Takata, N., Kawada, M., Muguruma, K., Sekiguchi, K., Saito, K., Yonemura, S., Eiraku, M., and Sasai, Y. (2012). Self-formation of optic cups and storable stratified neural retina from human ESCs. Cell Stem Cell *10*, 771–785.

Osakada, F., Ikeda, H., Mandai, M., Wataya, T., Watanabe, K., Yoshimura, N., Akaike, A., Akaike, A., Sasai, Y., and Takahashi, M. (2008). Toward the generation of rod and cone photoreceptors from mouse, monkey and human embryonic stem cells. Nat. Biotechnol. *26*, 215–224.

Phillips, M.J., Perez, E.T., Martin, J.M., Reshel, S.T., Wallace, K.A., Capowski, E.E., Singh, R., Wright, L.S., Clark, E.M., Barney, P.M., et al. (2014). Modeling human retinal development with patient-specific induced pluripotent stem cells reveals multiple roles for visual system homeobox 2. Stem Cells *32*, 1480–1492.

Rostovskaya, M., Fu, J., Obst, M., Baer, I., Weidlich, S., Wang, H., Smith, A.J., Anastassiadis, K., and Stewart, A.F. (2012). Transposon-mediated BAC transgenesis in human ES cells. Nucleic Acids Res. *40*, e150.

Rostovskaya, M., Naumann, R., Fu, J., Obst, M., Mueller, D., Stewart, A.F., and Anastassiadis, K. (2013). Transposon mediated BAC transgenesis via pronuclear injection of mouse zygotes. Genesis *51*, 135–141.

Shaham, O., Menuchin, Y., Farhy, C., and Ashery-Padan, R. (2012). Pax6: a multi-level regulator of ocular development. Prog. Retin. Eye Res. *31*, 351–376.

Zhong, X., Gutierrez, C., Xue, T., Hampton, C., Vergara, M.N., Cao, L.-H.H., Peters, A., Park, T.S., Zambidis, E.T., Meyer, J.S., et al. (2014). Generation of three-dimensional retinal tissue with functional photoreceptors from human iPSCs. Nat. Commun. *5*, 4047.